CHINESE OPTICS LETTERS

Vol. 20, No. 6 | June 2022

On-chip short-wave infrared multispectral detector based on integrated Fabry–Perot microcavities array

Zhiyi Xuan (玄志一)[1,2,3,4], Qingquan Liu (刘清权)[1,2,3,4], Zhuangzhuang Cui (崔壮壮)[1,2,4], Songlei Huang (黄松垒)[2,5], Bo Yang (杨 波)[2,3], Chenlu Li (李辰璐)[1,2,3,4], Shaowei Wang (王少伟)[1,2,4,6*], and Wei Lu (陆 卫)[1,2,3,4**]

[1] State Key Laboratory of Infrared Physics, Shanghai Institute of Technical Physics, Chinese Academy of Sciences, Shanghai 200083, China

[2] University of Chinese Academy of Sciences, Beijing 100049, China

[3] School of Physical Science and Technology, ShanghaiTech University, Shanghai 201210, China

[4] Shanghai Research Center for Quantum Sciences, Shanghai 201315, China

[5] State Key Laboratories of Transducer Technology, Shanghai Institute of Technical Physics, Chinese Academy of Sciences, Shanghai 200083, China

[6] Nantong Academy of Intelligent Sensing, Nantong 226000, China

*Corresponding author: wangshw@mail.sitp.ac.cn

**Corresponding author: luwei@mail.sitp.ac.cn

Received January 22, 2022 | Accepted March 22, 2022 | Posted Online April 27, 2022

We demonstrate an ultra-compact short-wave infrared (SWIR) multispectral detector chip by monolithically integrating the narrowband Fabry–Perot microcavities array with the InGaAs detector focal plane array. A 16-channel SWIR multispectral detector has been fabricated for demonstration. Sixteen different narrowband response spectra are acquired on a 64×64 pixels detector chip by four times combinatorial etching processes. The peak of the response spectra varies from 1450 to 1666 nm with full width at half-maximum of 24 nm on average. The size of the SWIR multispectral detection system is remarkably reduced to a 2 mm^2 detector chip.

Keywords: short-wave infrared; detector; multi-spectra; micro-cavity; on-chip.

DOI: 10.3788/COL202220.061302

1. Introduction

Spectroscopy information is widely used to identify different matter and has a lot of applications, such as sensors[1,2], multispectral detection[3–6], and remote sensing[7,8]. For conventional multispectral detection systems[9,10], their wavelength division device and detector are separated and require mechanical or electrical scanning to obtain different spectral information. Most of the commercialized detectors have no ability to obtain spectral information by themselves. Wavelength division devices, such as a grating, prism, and Michelson interferometer, enable the detection system to identify the light wavelength precisely. However, the spectrum acquisition systems based on them are complex with large footprint and lead to heavy load and looseness[11,12]. They are unsuitable for on-site or portable application areas. To minimize the volume of spectrum acquisition systems, a multi-color detector has been developed by integrating different waveband detection structures vertically to get two or more broadband spectral signals simultaneously[13,14]. However, the multi-color detector is a longitudinal laminated structure with a certain degree of optical and electronic crosstalk. The spectral resolution is too low due to its broadband response. In addition, some filter-free detectors with a tunable narrowband response spectrum have been developed, such as organic photodetectors[15–17]. These filter-free strategies have a small footprint, but it is not easy to increase the number of spectral channels to tens or even hundreds. Therefore, a miniature wavelength division device integratable with detectors is the key to reducing the footprint of multispectral and hyperspectral detection systems. To this end, ultra-compact wavelength division devices based on nanophotonic principles, such as metasurface, photonic crystal, and plasmonic structure, have been widely investigated[18–25]. For example, researchers bond the photonic crystal slab on the charge-coupled device (CCD) or complementary metal oxide semiconductor (CMOS) detector to form a chip-level spectrometer [26–31] in the visible. It remarkably reduces the footprint of the spectrum acquisition system. However, the minimum size of metasurface structure is less than 1 μm. It needs highly precise and high-cost fabrication processes like e-beam lithography, which increases the fabrication difficulty and cost enormously. Additionally, no pixel-level wavelength division devices monolithically integrated with a detector in the short-wave infrared (SWIR) have been reported, to the best of our knowledge. Only a dual-waveband SWIR

InGaAs focal plane array (FPA) with broad bands of 46 nm and 54 nm has been developed by integrating two filters [32].

In this work, we propose a new SWIR multispectral detector chip by monolithically integrating a Fabry–Perot (FP) microcavities array on an InGaAs FPA, which can acquire multiple narrowband spectral signals itself with an ultra-compact footprint. Meanwhile, it has no moving parts and is portable and stable.

2. Experiment

We proposed and developed a new type of wavelength division device based on the integrated narrow bandpass filters[25,30]. FP cavities using a distributed Bragg reflector (DBR) with all-dielectric materials have low loss, high efficiency and are with narrowband, which is very suitable for narrowband optical detection. By changing the cavity layer thickness of the FP cavity, the transmission spectral peak can shift as designed. Here, we fabricated the FP microcavities array directly on the InGaAs FPA. Each detector pixel aligns with an FP microcavity by UV lithography. Therefore, the wavelength division structure monolithically integrates with the detector chip. The spectral acquiring system's footprint can be remarkably reduced to chip-level, and the stability is correspondingly increased. Only the light coupling with the transmission mode of FP microcavity can be received by the corresponding pixels, enabling different detector pixels to respond to different wavelengths of light. The current techniques can fabricate the FP cavities on a micro-scale by combining lithography and etching processes, with minimum size equal to one detector pixel. The FP cavities can be designed and integrated as an array with different narrow passbands on the pixel level[12,21]. Furthermore, different from the metasurface and grating, which work with diffraction and scattering principles, the light interference in the FP cavity results in a superior narrowband spectrum.

Figure 1(a) shows the schematic diagram of a monolithic integrated multispectral InGaAs detector. The detector chip comprises two parts: one is the 64 × 64 pixels InGaAs FPA, whose origin spectral response range is from 900 to 1700 nm; the other is the monolithic integrated FP microcavities array, which is directly fabricated on the backside of the InGaAs FPA. The film stacks of the FP microcavity can be described as

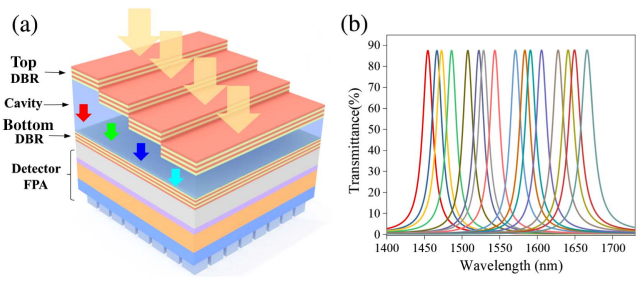

Fig. 1. (a) Schematic diagram of the FP microcavities array directly integrated on an InGaAs detector. (b) Simulated spectra of 16 FP microcavities array directly integrated on the InGaAs FPA.

$(LH)^3 2.37L (HL)^3$, which can be designed in detail according to our previous work[33]. H and L represent high and low refractive index materials with optical thickness of a quarter of the designed wavelength λ_0. The theoretical physical thicknesses of H and L are $\lambda_0/(4n_H)$ and $\lambda_0/(4n_L)$. We selected Si and SiO_2 as H and L layers with refractive indices of 2.53 and 1.46, respectively. The experimental physical thickness of each SiO_2 (L) and Si (H) layer is 291 nm and 136 nm, respectively. The initial cavity layer is designed as 2.37L to enable the right spectrum peak to locate at l666 nm, and other spectral channels blue shift with the reduction of cavity layer thickness. The number of DBR stacks (LH) or the thickness of the cavity layer can tune the bandwidth and spectral resolution of the filter: the larger number of DBR stacks (LH), the higher the spectral resolution of the structure. The reason for choosing Si and SiO_2 as high and low refractive index materials is to get large refractive index difference and have wide spectral tunable range. Other materials like TiO_2, Ta_2O_5, can also be selected as high refractive index material in the SWIR range. SiO, ZnS, etc., can also be selected as low refractive index material in the SWIR range. In these materials, the refractive index difference of Si and SiO_2 is the largest, but the absorption of Si is also relatively large, leading to low transmittance. The absorption is low with high transmittance when the refractive index difference is small with other materials. Hence, different choices and combinations of materials can be made according to different application requirements. By changing the cavity thickness of each FP cavity in different pixel areas, the transmission peak can be tuned to different wavelengths. The simulation spectra of this structure are shown in Fig. 1(b). Here, we designed 16 response spectra of the detector by integrating different thicknesses of each FP cavity for demonstration.

The fabrication process is illustrated in Fig. 2. The Si and SiO_2 layers are deposited on the backside of the InGaAs detector by using an electron beam evaporation system (Leybold ARES1110) with vacuum of 1.6×10^{-4} mbar (1 mbar = 100 Pa) and temperature of 100°C, where the evaporation speed for SiO_2 is 48 nm/min, and for Si is 12.6 nm/min. The bottom DBR stacks and cavity layer of $(LH)^3 2.37L$ are deposited firstly. Then, the cavity layer is processed with combinatorial etching processes. Sixteen cavities with different thicknesses are fabricated with only four times of UV lithography (MJB4, SUSS Mask aligner05080104) and inductively coupled plasma (ICP, Oxford PlasmaPro System 100) etching process. The two gases used for etching were argon (Ar) and trifluoromethane (CHF_3) with a flow rate ratio of 1:3. The radio frequency (RF) power and ICP power were set as 50 W and 80 W, respectively. In addition to the combinatorial etching process, the FP microcavities array can also be realized by using combinatorial deposition processes[34]. Lastly, the top DBR stacks of $(HL)^3$ are deposited on the structure. The FP microcavities array is monolithically integrated onto the InGaAs detector chip. A representative cross-sectional scanning electron microscopy (SEM) image of the monolithic integrated FP microcavity is shown in Fig. 3(a) to verify the accuracy of our experiment. The incident light is

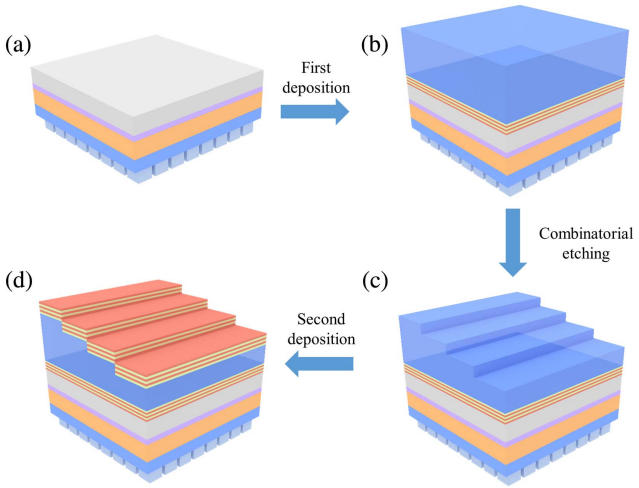

Fig. 2. Fabrication process of on-chip InGaAs multispectral detector. (a) The InGaAs FPA. (b) The bottom DBR and cavity layer are deposited on the InGaAs FPA. (c) The cavity layer is processed with UV lithography and ICP etching. (d) The top DBR is deposited on the processed cavity layer and forms 16 different FP microcavities.

filtered by the FP microcavity and absorbed by the InGaAs detector pixel, then converted to the electrical signal, and output by the readout circuits (ROIC). The picture of the fabricated 16-channel multispectral detector chip with ROIC is shown in Fig. 3(b). Meanwhile, its detector pixels on the former side and the FP microcavities array on the backside are correspondingly aligned during the lithography process. Figure 3(c) is the image of the 64 × 64 pixels InGaAs detector FPA. Figure 3(d) is the monolithically integrated FP cavities array, and 16 different optical channels are separated by the diaphragms (Au with 100 nm thickness) of yellow areas. During the combinatorial etching processes, the diaphragms work as a buffer area between channels to prevent crosstalk etching.

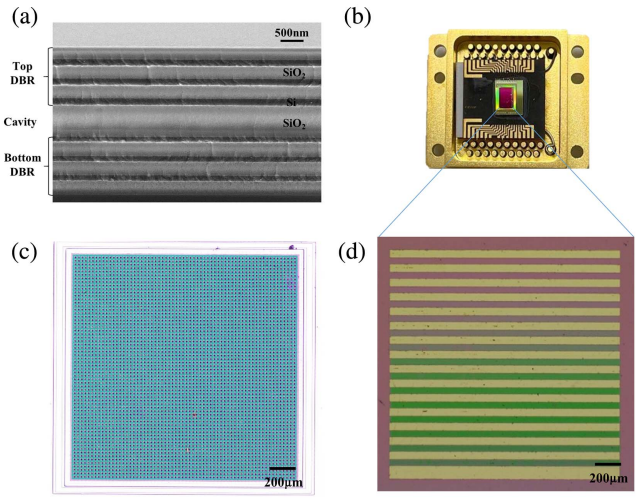

Fig. 3. (a) Cross-section SEM image of a representative monolithic integrated FP cavity with structure of $(LH)^3 2.37L(HL)^3$, where H is the Si layer, and L is the SiO_2 layer. (b) The picture of the fabricated 16-channel multispectral detector chip with ROIC of the size about 2 mm^2. (c) The 64 × 64 pixels InGaAs detector FPA. (d) The 16-channel FP microcavities array, which is monolithically integrated with the detector chip.

3. Results and Discussion

After the monolithic integrated process, the multispectral detector chip is bonded with ROIC [Fig. 3(a)]. The total footprint of the fabricated 16-channel multispectral detector chip is about 2 mm^2, which is minimum and much smaller than the size of conventional infrared multispectral system. The spectral response of the fabricated 16-channel multispectral detector is measured by a monochromator with a collimator, as shown in Fig. 4(a). Meanwhile, the same type of standard InGaAs FPA is measured by the same system as a comparison. The response spectra of the reference standard detector and the fabricated multispectral detector are shown in Figs. 4(b) and 4(c). The response spectrum of the standard InGaAs FPA is broadband from 900 to 1700 nm. In contrast, the monolithically integrated multispectral InGaAs FPA has 16 distinct response spectra on different pixels. The peaks of the measured 16 different response narrowband spectra are 1666, 1649, 1642, 1628, 1606, 1591, 1584, 1571, 1543, 1529, 1522, 1508, 1486, 1473, 1467, and 1454 nm.

As designed, each channel of our multispectral detector has a unique narrowband response spectrum. The peaks of these 16-channel response spectra are separated and enable each detector channel to detect different specific wavelengths of light. Moreover, the channel number of the multispectral detector chip can be increased exponentially by increasing the times of the combinatorial etching process. Experimentally, the full width at half-maximum (FWHM) reaches 24 nm on average, which can be narrowed by adding the DBR stack to be as narrow as 1 nm[30] or even narrower, and meets the needs of many multispectral detection fields. The difference between simulation and experimental results is mainly caused by the fabrication

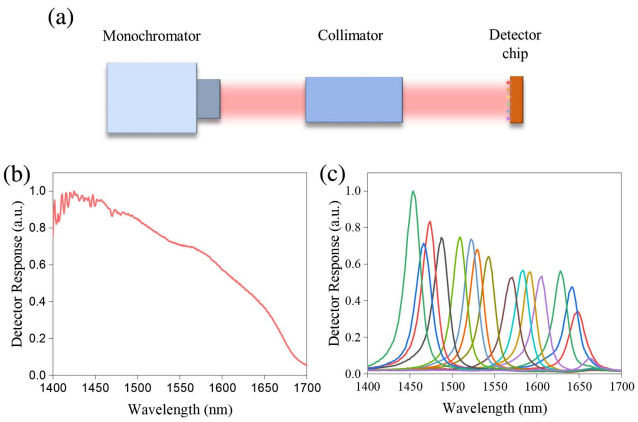

Fig. 4. (a) Schematic diagram of the InGaAs FPA response spectrum test system. (b) The measured response spectrum of the standard detector. (c) The measured response spectra of the 16-channel multispectral detector.

processes. The FWHM and transmittance of the FP cavities array are directly affected by the n (refractive index) and k (extinction coefficient) values of the materials. The vacuum and temperature of the coating process can influence the n and k values of the films. The experimental FP microcavities array is directly fabricated onto the InGaAs FPA. Hence, the measured 16-channel response spectra of this multispectral detector chip are the combined results of the FP cavities array spectra [Fig. 1(b)] and InGaAs detector response spectrum [Fig. 4(b)]. For instance, the low response intensity of the last channel (spectrum peak at 1666 nm) comes from the intrinsic low responsivity of the InGaAs detector itself, as shown in Fig. 4(c).

Indeed, the multispectral detector chips with narrowband response spectra are helpful for infrared spectral detection. Increasing the number of DBR layers or adopting material with a higher refractive index difference can narrow the bandwidth of the response spectrum. Furthermore, increasing the maximum etching depth and etching times of the fabrication process will increase the spectral range and the channel number of multispectral detector chips, respectively. The response channels of 1649, 1606, 1571, 1529, 1454 nm correspond to the absorption peak of gases CH_4, H_2S, CO, C_2H_2, CO_2, respectively. Since many gases have characteristic absorption spectra in the SWIR range, such a multispectral detector chip can work as a sensor and multispectral imager. The peaks of response spectra can be designed and controlled to gas absorption wavelengths for the application of the non-dispersive infrared (NDIR) multi-gas sensor. In addition, an ultra-compact multispectral image camera can be realized with the help of a push-broom setup on such a detector chip or construction of a wavelength division structure by using different channels super-pixel arrays.

4. Conclusions

In conclusion, we have demonstrated a novel SWIR multispectral detector chip by monolithically integrating the narrowband FP microcavities array with the InGaAs FPA. Each FP microcavity and the corresponding detector pixels are integrated and aligned using UV lithography. The multispectral detector chip can distinguish 16 different SWIR wavelengths by itself. The response spectra of each detector pixel can be adjusted flexibly by changing the thickness of the cavity layer. The spectral channels can be increased to 128 by only seven times of combinatorial etching. The monolithically integrated detector chip without moving elements is portable and stable, remarkably reducing the footprint of the multispectral detection system to a 2 mm^2 size. It is promising for practical applications such as multispectral infrared imaging in smartphones, object identification in automatic drive, and real-time monitoring of multiple gases in the industrial fields.

Acknowledgement

This work was supported by the National Natural Science Foundation of China (NSFC) (No. 11874376), Shanghai Science and Technology Foundations (Nos. 19DZ2293400 and 19ZR1465900), Shanghai Municipal Science and Technology Major Project (No. 2019SHZDZX01), and Chinese Academy of Sciences President's International Fellowship Initiative (No. 2021PT0007).

References

1. X. Tan, H. Zhang, J. Li, H. Wan, Q. Guo, H. Zhu, H. Liu, and F. Yi, "Non-dispersive infrared multi-gas sensing via nanoantenna integrated narrowband detectors," Nat. Commun. **11**, 5245 (2020).
2. J. Mayrwoeger, W. Reichl, C. Krutzler, and B. Jakoby, "Measuring CO_2 concentration with a Fabry-Perot based bolometer using a glass plate as simple infrared filter," Sens. Actuator B Chem. **170**, 143 (2012).
3. C. D. Tran, "Infrared multispectral imaging: principles and instrumentation," Appl. Spectrosc. Rev. **38**, 133 (2003).
4. M. Mrejen, Y. Erlich, A. Levanon, and H. Suchowski, "Multicolor time-resolved upconversion imaging by adiabatic sum frequency conversion," Laser Photon. Rev. **14**, 2000040 (2020).
5. Z. Zhou, T. Zhou, S. Zhang, Z. Shi, Y. Chen, W. Wan, X. Li, X. Chen, S. N. Gilbert Corder, Z. Fu, L. Chen, Y. Mao, J. Cao, F. G. Omenetto, M. Liu, H. Li, and T. H. Tao, "Multicolor T-ray imaging using multispectral metamaterials," Adv. Sci. **5**, 1700982 (2018).
6. F. M. Paul, B. Paul Stuart, D. B. Jeffrey, G. F. Dale, S. H. Andrew, and A. W. Edward, "Comparison of flash lidar detector options," Opt. Eng. **56**, 031223 (2017).
7. H. Aasen, E. Honkavaara, A. Lucieer, and P. J. Zarco-Tejada, "Quantitative remote sensing at ultra-high resolution with UAV spectroscopy: a review of sensor technology, measurement procedures, and data correction workflows," Remote Sens. **10**, 1091 (2018).
8. R. Mannila, C. Holmlund, H. Ojanen, A. Näsilä, and H. Saari, "Short-wave infrared (SWIR) spectral imager based on Fabry-Perot interferometer for remote sensing," Proc. SPIE **9241**, 92411M (2014).
9. F. D. van der Meer, H. M. A. van der Werff, F. J. A. van Ruitenbeek, C. A. Hecker, W. H. Bakker, M. F. Noomen, M. van der Meijde, E. J. M. Carranza, J. B. de Smeth, and T. Woldai, "Multi- and hyperspectral geologic remote sensing: a review," Int. J. Appl. Earth Obs. Geoinf. **14**, 112 (2012).
10. L. Guolan and F. Baowei, "Medical hyperspectral imaging: a review," J. Biomed. Opt. **19**, 010901 (2014).
11. J. Liu, J. Chen, J. Liu, S. Feng, X. Li, and J. Cui, "Optical design of a prism-gating-based lenslet array integral field spectrometer," Opt. Express **26**, 19456 (2018).
12. Z. Xuan, Y. Zhi, S. Wang, Y. Zhang, Y. Zheng, J. Li, F. Liu, Y. Xie, Y. Chen, W. Shi, F. Yi, and W. Lu, "Rapid and precise wavelength determination approach based on visually patterned integrated narrow bandpass filters," IEEE Photonics J. **11**, 4900307 (2019).
13. A. Jdidi, N. Sfina, S. Abdi-Ben Nassrallah, M. Said, and J. L. Lazzari, "A multicolor quantum well photodetector for mid- and long-wavelength infrared detection," Semicond. Sci. Technol. **26**, 125019 (2011).
14. S. Ogawa and M. Kimata, "Wavelength- or polarization-selective thermal infrared detectors for multi-color or polarimetric imaging using plasmonics and metamaterials," Materials **10**, 493 (2017).
15. K. Yang, J. Wang, Z. Zhao, Y. Sun, M. Liu, Z. Zhou, X. Zhang, and F. Zhang, "Highly sensitive photomultiplication type polymer photodetectors by manipulating interfacial trapped electron density," Chem. Eng. J. **435**, 134973 (2022).
16. Z. Zhao, M. Liu, K. Yang, C. Xu, Y. Guan, X. Ma, J. Wang, and F. Zhang, "Highly sensitive narrowband photomultiplication-type organic photodetectors prepared by transfer-printed technology," Adv. Funct. Mater. **31**, 2106009 (2021).
17. M. Liu, J. Wang, K. Yang, Z. Zhao, Z. Zhou, Y. Ma, L. Shen, X. Ma, and F. Zhang, "Highly sensitive, broad-band organic photomultiplication-type photodetectors covering UV-Vis-NIR," J. Mater. Chem. C **9**, 6357 (2021).
18. J. W. Stewart, J. H. Vella, W. Li, S. H. Fan, and M. H. Mikkelsen, "Ultrafast pyroelectric photodetection with on-chip spectral filters," Nat. Mater. **19**, 158 (2020).

19. B. Feng, J. Y. Zhu, B. R. Lu, F. F. Liu, L. Zhou, and Y. F. Chen, "Achieving infrared detection by all-Si plasmonic hot-electron detectors with high detectivity," ACS Nano **13**, 8433 (2019).
20. A. Cordaro, H. Kwon, D. Sounas, A. F. Koenderink, A. Alu, and A. Polman, "High-index dielectric metasurfaces performing mathematical operations," Nano Lett. **19**, 8418 (2019).
21. Z. Xuan, J. Li, Q. Liu, F. Yi, S. Wang, and W. Lu, "Artificial structural colors and applications," The Innovation **2**, 100081 (2021).
22. X. He, Y. Liu, K. Ganesan, A. Ahnood, P. Beckett, F. Eftekhari, D. Smith, M. H. Uddin, E. Skafidas, A. Nirmalathas, and R. R. Unnithan, "A single sensor based multispectral imaging camera using a narrow spectral band color mosaic integrated on the monochrome CMOS image sensor," APL Photonics **5**, 046104 (2020).
23. C. Williams, G. S. D. Gordon, T. D. Wilkinson, and S. E. Bohndiek, "Grayscale-to-color: scalable fabrication of custom multispectral filter arrays," ACS Photonics **6**, 3132 (2019).
24. Y. Liang, S. Zhang, X. Cao, Y. Lu, and T. Xu, "Free-standing plasmonic metal-dielectric-metal bandpass filter with high transmission efficiency," Sci. Rep. **7**, 4357 (2017).
25. S. W. Wang, D. Q. Liu, B. Lin, X. S. Chen, Z. F. Li, Y. Shi, W. Wang, and W. Lu, "Realization of integrated narrow bandpass filters in the infrared region," Int. J. Infrared Millim. Waves **25**, 1677 (2004).
26. D. Pohl, M. R. Escale, M. Madi, F. Kaufmann, P. Brotzer, A. Sergeyev, B. Guldimann, P. Giaccari, E. Alberti, U. Meier, and R. Grange, "An integrated broadband spectrometer on thin-film lithium niobate," Nat. Photonics **14**, 24 (2020).
27. J. Meng, J. J. Cadusch, and K. B. Crozier, "Detector-only spectrometer based on structurally colored silicon nanowires and a reconstruction algorithm," Nano Lett. **20**, 320 (2020).
28. S. N. Zheng, J. Zou, H. Cai, J. F. Song, L. K. Chin, P. Y. Liu, Z. P. Lin, D. L. Kwong, and A. Q. Liu, "Microring resonator-assisted Fourier transform spectrometer with enhanced resolution and large bandwidth in single chip solution," Nat. Commun. **10**, 2349 (2019).
29. Z. Wang, S. Yi, A. Chen, M. Zhou, T. S. Luk, A. James, J. Nogan, W. Ross, G. Joe, A. Shahsafi, K. X. Wang, M. A. Kats, and Z. F. Yu, "Single-shot on-chip spectral sensors based on photonic crystal slabs," Nat. Commun. **10**, 6 (2019).
30. S.-W. Wang, C. Xia, X. Chen, W. Lu, M. Li, H. Wang, W. Zheng, and T. Zhang, "Concept of a high-resolution miniature spectrometer using an integrated filter array," Opt. Lett. **32**, 632 (2007).
31. Z. Yang, T. Albrow-Owen, W. Cai, and T. Hasan, "Miniaturization of optical spectrometers," Science **371**, 480 (2021).
32. H. J. Tang, X. Li, Y. J. Wang, W. B. Duan, X. M. Shao, and H. M. Gong, "The novel dual-waveband SWIR InGaAs FPAs with monolithic integration filter microstructure," Proc. SPIE **8982**, 898229 (2014).
33. S. W. Wang, X. S. Chen, W. Lu, L. Wang, Y. G. Wu, and Z. S. Wang, "Integrated optical filter arrays fabricated by using the combinatorial etching technique," Opt. Lett. **31**, 332 (2006).
34. S. W. Wang, M. Li, C. S. Xia, H. Q. Wang, X. S. Chen, and W. Lu, "128 channels of integrated filter array rapidly fabricated by using the combinatorial deposition technique," Appl. Phys. B-Lasers Opt. **88**, 281 (2007).